Multiphysics Modeling of Magnetoelectric Composite Disks by a 2D Axisymmetric Finite Element Approach

S. Karimi and H. Talleb

Sorbonne Université, CNRS, Laboratoire de Génie Electrique et Electronique de Paris, 75252, Paris, France
Université Paris-Saclay, CentraleSupélec, CNRS, Laboratoire de Génie Electrique et Electronique de Paris, 91192, Gif-sur-Yvette, France.
E-mail: sheno.karimi@sorbonne-universite.fr

A 2D axisymmetric finite element multiphysics model is proposed to study magnetoelectric composite disks. This modeling approach includes a nonlinear magneto-elastic model to replicate the behavior of magnetostrictive materials under static conditions. Additionally, it offers a harmonic regime resolution that considers frequency dependence, including the implicit inclusion of eddy currents in the formulation, as well as electrical load. To validate the model, simulation results regarding the dependence of the static magnetic field and frequency are presented and compared with experimental measurements from literature.

***Index Terms*—Piezoelectric, magnetostriction, magnetoelectric composite, eddy current, energy harvesting, finite element modeling, nonlinearity, edge element, multiphysics model.**

I. Introduction

LAMINATED magnetoelectric composites (MECs) are engineered multifunctional materials composed of layers of piezoelectric and magnetostrictive materials. These materials indirectly couple electric and magnetic polarizations through the elastic phase. Unlike piezoelectric materials, magnetostrictive materials exhibit nonlinear behavior. Therefore, the preferred operational mode involves the application of an external magnetic field $\boldsymbol{H} = \boldsymbol{H}_{dc} + \boldsymbol{h}_{ac}$, where$\boldsymbol{H}_{dc}$ is a stable static bias, and $\boldsymbol{h}_{ac}$ is a small harmonic component. This magnetic field excitation induces substantial elastic stress within the magnetostrictive layers, resulting in strain across the piezoelectric layer and generating a harmonic electrical voltage V across its electrodes. Under resonance conditions, this harmonic electrical voltage V can be significant in MECs.

The performance of MECs is assessed using the magnetoelectric voltage coefficient $\tilde{\alpha}_V = \delta V/\delta h_{ac}$ or the magnetoelectric electric field coefficient $\tilde{\alpha}_E = \delta V/(t_p \delta h_{ac})$, where t_p represents the thickness of the piezoelectric layer. The effectiveness of MECs depends on the orientation of the external magnetic field H concerning the longitudinal (L) or transverse (T) magnetization and polarization directions of the magnetostrictive and piezoelectric layers, resulting in different modes like LT, LL, TT, TL modes [1]. Due to their compact size and high-power efficiency, MECs have gained significant attention in various engineering applications, including magnetic sensors, energy transducers [2-4], and potential biomedical solutions [5]. Among the most promising structures, composites based on Terfenol-D and PZT layers [6-7] have demonstrated excellent performance. However, Terfenol-D/PZT composites suffer from losses caused by mechanical losses due to the epoxy adhesive used to bond the material layers and the presence of eddy currents, particularly given the high conductivity of Terfenol-D ~ 610^6 S/m [8]. Moreover, there's an environmental concern as Terfenol-D and PZT materials are known to be environmentally toxic, which raises questions about their extensive use. In this context, while there has been a preference for environmentally friendly alternatives such as magnetostrictive FeGa alloys (Galfenol) or piezoelectric materials like $BaTiO_3$ (barium titanate, called BTO here) [9-11], it's essential to critically evaluate and explore these alternatives considering their environmental impact and performance characteristics.

To achieve innovative and optimized designs for future MECs while reducing costs and development time, it is crucial to employ multiphysics modeling that considers all physical coupling phenomena, including losses, regardless of the structural form under investigation. While analytical methods like equivalent electrical circuits and numerical codes such as the Finite Element Method (FEM) based on multiphysics constitutive laws are valuable tools, analytical methods relying on equivalent electrical circuits are limited to 1D assumptions and fail to accurately represent the complex interactions within ME composites or account

for the electrical impact on the magneto-elastic phase when the structure is subjected to electrical impedance. Recently, a 3D FEM model [12], utilizing a complete ***A-V*** formulation (combining mixed magnetic vector potential A and electric scalar potential ***V***) along with nodal and edge Whitney elements, has been effectively employed to study laminated magnetoelectric composite (LMEC) disks under the TT and LT modes while considering the electrical load impedance and eddy current effects. Although the simulation results have shown good concordances with the measurement concerning a Galfenol/BTO/Galfenol disk, the computational time can be excessive in harmonic regime. To overcome this challenge, this paper proposes transposing the A-V formulation into a 2D axisymmetric case, as depicted in Figure 1.

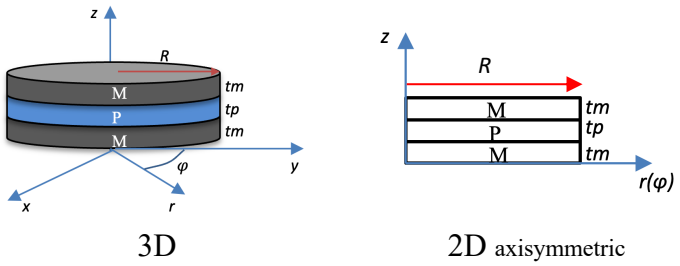

Figure 1: Illustration of the magnetoelectric composite disk in both 3D and 2D axisymmetric cases, represented in cylindrical coordinates$\{e_r, e_\varphi, e_z\}$. The composite disk consists of one piezoelectric layer (P) and two magnetostrictive layers (M), with the radius denoted as R. The thicknesses of the magnetostrictive and piezoelectric layers are denoted as t_m and t_p, respectively.

The paper is structured into five sections. In Section II, we introduce the nonlinear model of the magnetostrictive material, which includes comparisons between Galfenol and Terfenol-D, along with experimental results for validation. Section III elaborates on the complete finite element formulation of the 2D axisymmetric multiphysics magnetoelectric problem. In Section IV, we compare the simulation results in the TT-mode with experimental data from the literature. Finally, Section V offers the study's conclusion.

II. THE NONLINEAR MAGNETO-ELASTIC MODEL

To introduce this section, it's important to highlight that in problems involving MECs, the ferroelectric properties of the piezoelectric material, such as permittivity and piezoelectric coefficients, are typically considered linear. In contrast, the ferromagnetic properties of the magnetostrictive material, which include permeability and piezomagnetic coefficients, demonstrate nonlinearity concerning magnetization and magnetostriction. This nonlinearity stems from the fact that the properties of the magnetostrictive material at a specific location are influenced by the state variables at that location. As a result of spatial variations in stress and magnetic field, these material coefficients exhibit spatial non-uniformity and are influenced by the applied static field.

Hence, when evaluating the magnetoelectric response, it is imperative to account for the non-uniformity within the composite stemming from material's nonlinearity. To address this challenge, the applied magnetic excitation $\boldsymbol{H}$ (A/m**)** in the field problem is split into a small harmonic component $\boldsymbol{h}_{ac}$ while maintaining an optimal static bias $\boldsymbol{H}_{dc}$. This approach necessitates a two-step solution within the modeling framework. In the initial phase, which pertains to the static regime, incremental piezomagnetic and permeability coefficients of the magnetostrictive material are computed for each material zone at the chosen static bias point. Typically, this phase employs a nonlinear model based on a magneto-elastic framework [13-19].

The second step pertains to the harmonic regime, where the frequency-dependent magnetoelectric voltage coefficient $\tilde{\alpha}_V$ is determined using a small signal linear approximation around the optimal static bias $\boldsymbol{H}_{dc}$. This is accomplished through a nonlinear process, such as the Newton-Raphson method or a piecewise linear decomposition [19] applied in this context. Here, we utilize the piecewise linear decomposition proposed in [19].

A. The magnetization model.

In the existing literature, several magneto-elastic multiscale anhysteretic models, based on Gibbs free energy, have been put forward for integration into the finite element modeling framework [19-23]. These models offer diverse approaches, including the utilization of an analytical expansion with higher-order terms in the Taylor series [14], the application of the Discrete Energy-Averaged Model (DEAM) [15-16], or the adoption of simplified magneto-elastic Gibbs free energy relations where bulk magnetization and strain are derived as expected values from a large number of potential moment orientations, using an energy-based probability density function [19][24-26]. Each approach has its own merits and limitations, and the choice is contingent upon the specific requirements of the analysis.

Regardless of the chosen model, the primary focus remains on two crucial coefficients: the incremental piezomagnetic coefficient tensor and the permeability coefficient tensor. These coefficients play a vital role in characterizing the nonlinear behavior of the magnetostrictive material within the magnetoelectric composite structure.

Here, we propose a simplified method for the direct determination of these tensors. This approach is based on a model that relies on the following magnetoelastic constitutive law for the magnetic induction $\boldsymbol{B}$ (Wb/m^2):

$$\boldsymbol{B}(H,T) = \mu\boldsymbol{H} + d\boldsymbol{T} \tag{1}$$

where μ (H/m) and d (nA/m) represent the permeability and the piezomagnetic coefficients of the material. $\boldsymbol{T}$ represents the stress inside the material such as $d\boldsymbol{T} = \mu_o\boldsymbol{M}(T)$.

In considering $\mu\boldsymbol{H} = \mu_o\big(\boldsymbol{H} + \boldsymbol{M}(H)\big)$ the constitutive law can be rewritten as follows:

$$\boldsymbol{B}(H,T) = \mu_o\big(\boldsymbol{H} + \boldsymbol{M}(H,T)\big) \tag{2}$$

where μ_o is the vaccum permeability (H/m).

When a magnetostrictive material is exposed to both stress and a magnetic field, specifically along the easy axis direction (z-direction), its magnetization and magnetostriction anhysteretic behaviors under pre-stresses can be determined by averaging across all potential directions, as outlined by [26]. Despite recent proposals for analytical solutions to magnetization and magnetostriction anhysteretic behaviors [19], their expressions pose a numerical challenge due to the utilization of the Dawson function, resulting in a divergence issue, particularly concerning the coupling value between magnetic field and mechanical stress [19]. Preceding this, a simplified model (3-a) from [27] has been proposed by accounting for only six domains as possible directions and an equivalent stress T_{eq} equivalent to the magnitude of the total stress $\boldsymbol{T}$. The detailed demonstration is provided in Appendix A.

$$\boldsymbol{M}(H,T) = M_s \frac{\sinh(\kappa\boldsymbol{H})}{\cosh(\kappa\boldsymbol{H}) + \frac{2}{\exp(\alpha.T)}} \tag{3}$$

where, $\kappa = A_s \mu_o M_s$, $\alpha = \frac{3}{2}\lambda_s A_s$, M_s and λ_s are the magnetization and magnetostriction saturations. The parameter A_s (mJ/m^3) can be related to the initial anhysteretic $\chi_o = \partial_H \boldsymbol{M})_{\boldsymbol{H}=\boldsymbol{0}}$ susceptibility such as [26-27]:

$$A_s = \frac{3\chi_o}{\mu_o {M_s}^2} \tag{4}$$

In practical terms, when subjected to a pre-stress, the initial anhysteretic susceptibility undergoes changes. Therefore, we suggest incorporating the pre-stress effect into the κ parameter by considering $\kappa(T) = A_s(T)\mu_o M_s$ where $A_s(T)$ is a function of the stress $\boldsymbol{T}$. Figure 2 illustrates the extraction of $A_s(T)$ using the analytical solution proposed in [19] for a Terfenol-D material under various pre-stresses $\boldsymbol{T}$.

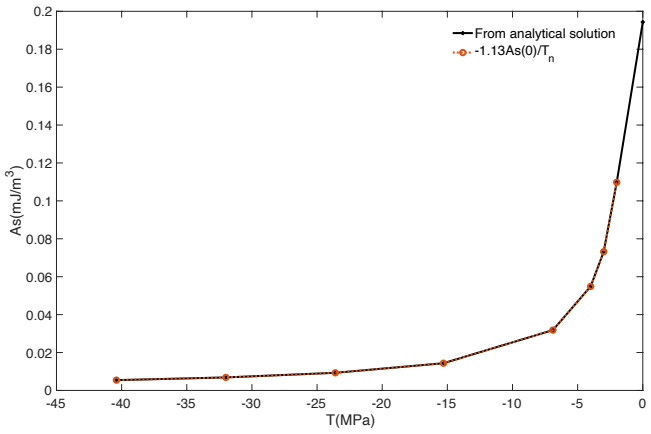

Figure 2: Evolution of the $A_s(T)$ parameter under pre-stresses $\boldsymbol{T}$ with the analytical solution from [19]

We can notice that the parameter $A_s(T)$ can be expressed such as:

$$A_s(T) = -1.13As(0)/T_n \tag{5}$$

with $T_n = \boldsymbol{T}/[1\ \text{MPa}]$ and the coefficient 1.13 can vary depending on the material under study.

Equation (2) can be viewed as the combined contribution of the ferromagnetic component with $\tanh(\kappa \boldsymbol{H})$ and the magnetostriction component with $\frac{2}{\exp(\alpha.T)}$. Therefore, we can adopt the following simplified approach:

$$\boldsymbol{M}(H,T) = M_s \tanh(\kappa(T)\boldsymbol{H}) \tag{6}$$

An alternative method, suggested by [28] has introduced the same expression. Drawing inspiration from Curie's Law $\boldsymbol{M}(H,\theta) = M_s \tanh(\kappa(\theta)\boldsymbol{H})$, which reveals the correlation between magnetization and temperature θ by $\kappa(\theta) = \boldsymbol{H}/(\eta\theta)$ with $\eta = k_B/m$, where m is the magnetic moment and k_B is the Boltzmann's constant, we propose a comparable form of $\kappa(T) = 1/(\eta \mathrm{T})$ as recommended in [28] to associate the connection between magnetization and the magnitude of the total equivalent stress $\boldsymbol{T}$. Additionally, during the manufacturing of the disks, they undergo annealing under strong uniaxial compressive loads exceeding 200 MPa. Therefore, it is necessary to consider an intrinsic stress T_o [29], in addition to the externally applied stress T. Thus, the total stress T must be substituted by $(T + T_o)$, in this way $\kappa(T) = 1/\eta(T + T_o)$.

Through identification, the η parameter can be expressed by the relation:

$$\eta = \frac{1}{A_S(\mathrm{T})\mu_o M_S(T+T_o)} \tag{7}$$

Furthermore, the annealing process can induce a kinking phenomenon [28-30] due to the higher magnetocrystalline anisotropy of the sample. In this scenario, sharp regions in magnetization arise from the rapid growth of domains aligned parallel to the field at the expense of domains oriented perpendicular to it; this occurs through the motion of domain walls [31]. In such cases, as proposed by [29] for a material like Galfenol, the magnetization can be further modeled by incorporating a fractional fourth-order function term, as follows:

$$\boldsymbol{M}(H,T) = \Lambda + M_s \tanh(\boldsymbol{H}\zeta(T)) \tag{8}$$

where $\Lambda = \frac{\delta \boldsymbol{H}\zeta(T)}{\tau + (\boldsymbol{H}\zeta(T))^{\mathbf{4}}}$. δ and τ represent constant parameters depending on the measurement data.

In this context, for materials exhibiting a kinking phenomenon the η ,κ and τ parameters must be determined through curve fitting.

B. The incremental piezomagnetic and permeability coefficients

If the magnetoelastic excitation aligned with the easy axis magnetization, specifically in the z-direction (designated as the 3rd index), the piezomagnetic coefficient ${d_{33}}^H$ and the permeability coefficient ${\mu_{33}}^T$ are defined as follows:

$${d_{33}}^H = \partial_T \boldsymbol{B}|_H = \partial_T \boldsymbol{M}|_H(H,T) \tag{9}$$

$${\mu_{33}}^T = \partial_H \boldsymbol{B}|_T = \mu_o + \partial_H \boldsymbol{M}|_T(H,T) \tag{10}$$

By substituting $\theta = \boldsymbol{H}\zeta(T)$, we obtain:

$${d_{33}}^H = \mu_o \left[\partial_T \Lambda|_H - \frac{(\theta M_S)}{\bar{T}} \mathrm{sech}\,(\theta)^2\right] \tag{11}$$

$${\mu_{33}}^T = \mu_o \left[\partial_H \Lambda|_T + 1 + \frac{(\theta M_S)\mathrm{sech}\,(\theta)^2}{H}\right] \tag{12}$$

The expressions of $\partial_T \Lambda|_H$ and $\partial_H \Lambda|_T$ given in Appendix B represent the derivative forms of the fractional fourth-order function term Λ.

The permeability and piezomagnetic matrices can be expressed as follows, respectively:

$${\mu_{\mathrm{ij}}}^T = \mu_o \begin{pmatrix} {\mu_{11}}^T & 0 & 0 \\ 0 & {\mu_{22}}^T & 0 \\ 0 & 0 & {\mu_{33}}^T \end{pmatrix} \tag{13}$$

where ${\mu_{11}}^T = {\mu_{22}}^T = {\mu_{33}}^T$,

$$d_{ij}{}^{H} = \begin{bmatrix} 0 & 0 & d_{31}{}^{H} \\ 0 & 0 & d_{32}{}^{H} \\ 0 & 0 & d_{33}{}^{H} \\ 0 & d_{24}{}^{H} & 0 \\ d_{15}{}^{H} & 0 & 0 \\ 0 & 0 & 0 \end{bmatrix} \quad (14)$$

where $d_{31}{}^{H} = d_{32}{}^{H} = -d_{33}{}^{H}/2$ and $d_{14}{}^{H} = d_{15}{}^{H}$

To complete the piezomagnetic tensor, it is necessary to express the shear coefficient $d_{15}{}^{H}$. As mentioned in [31], determining the shear coefficient $d_{15}{}^{H}$ is not straightforward. Here, we present an approach to approximate it by considering the relationship between the shear direction and $m_i = M_i/M_s$ the direction cosines of the magnetization. For an isotropic magnetoelastic material, this relationship is expressed as [32]:

$$s_{13} = 3.\lambda_s m_1 m_3 \quad (15)$$

where λ_s is the magnetostriction saturation and $m_3 = \frac{\boldsymbol{M_3(T,H)}}{M_s} = \frac{\boldsymbol{M(T,H)}}{M_s}$.

The differential form of the shear direction according H_1 is given by :

$$ds_{13} = \left(\frac{ds_{13}}{dm_1}\right).\left(\frac{dm_1}{dH_1}\right) + \left(\frac{ds_{13}}{dm_3}\right).\left(\frac{dm_3}{dH_1}\right) \quad (16)$$

Where $\left(\frac{ds_{13}}{dm_{i=1,3}}\right) = 3.\lambda_s m_i$ and for a magnetically isotropic material, the cross-term $\frac{dm_3}{dH_1} = 0$ and $\frac{dm_1}{dH_1} = \frac{dM_1}{M_s dH_1} = \frac{\chi_1}{M_s}$, with χ_1 is the magnetic susceptibility expressed as :

$$\chi_1 = \frac{\mu_{11}{}^{T}}{\mu_o} - 1 \quad (17)$$

The piezomagnetic coefficient $d_{25}{}^{H}$ can be expressed as follows:

$$d_{15}{}^{H} = \mathbf{2}\partial_{H_1} s_{13}\big|_T = 2\left(\frac{ds_{13}}{dm_1}\right).\left(\frac{dm_1}{dH_1}\right) = 6.\lambda_s m_3 \frac{\chi_1}{M_s} = 6.\lambda_s \frac{\boldsymbol{M(T,H)}}{M_s^2}\left(\frac{\mu_{33}{}^{T}}{\mu_o} - 1\right) \quad (18)$$

In our nonlinear process, the incremental coefficients of interest are instead $q_{ij}{}^{H} = c_{ijkl}^{H} d_{ij}{}^{H}$ and $\mu_{\mathrm{ij}}{}^{S} = \mu_{\mathrm{ij}}{}^{T}(1-k^2)$.

where c_{ijkl}^{H} represents the elastics constants and k is the magneto-elastic coupling factor of the material such as $0.3<k<0.7$ for Galfenol [34-35] or $0.7< k< 0.75$ for Terfenol-D [36]. Here, we considered $k = 0.34$ and $k = 0.54$ for Galfenol and Terfenol-D respectively.

C. Validation of the nonlinear model

Figures 3 and 4 demonstrate the good agreement between the proposed model (solid lines) and the measurements conducted on cylindrical rods of Galfenol and Terfenol-D (indicated by diamond markers) as reported in [30] and [37]. These measurements were performed while considering the respective annealed built-in stresses, T_o = -50 MPa and T_o= -12 MPa. Consistent with the methodology outlined in reference [30], the -50 MPa value for Galfenol is established by initially considering the model with applied pre-stresses, specifically -5.5 MPa. Upon analyzing the Terfenol-D curves, adjustments were made, considering the -12 MPa value determined.

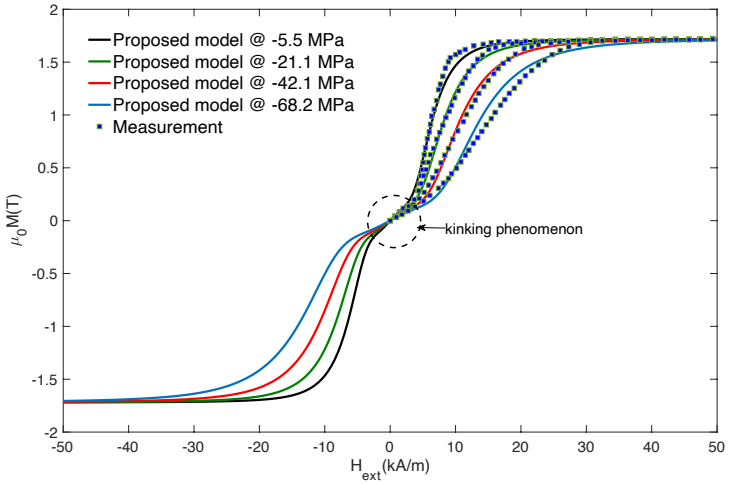

Figure 3: Magnetization curves under different uniaxial pre-stress T. Solid lines: proposed model @ T_o = -50 MPa with κ = -898640, τ =0.8415, η= -1.1555e-04. Diamond markers: measurements from [30]

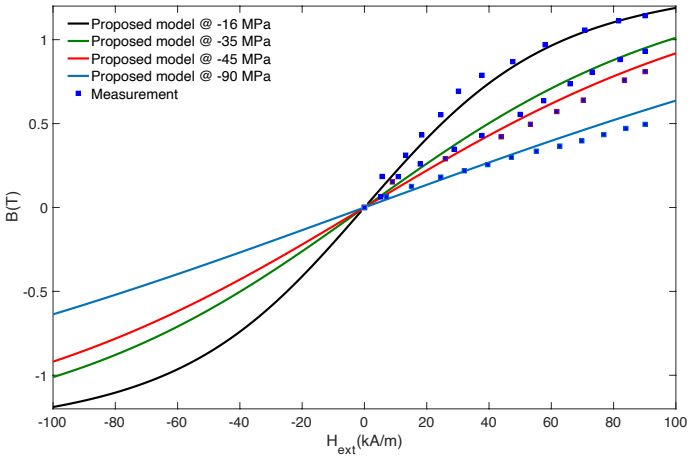

Figure 4: Magnetic induction curves under different uniaxial pre-stress T. Solid lines: proposed model @ T_o = -12 MPa with κ = 0, τ =0, η= -0.0020. Diamond markers: measurements from [37]

Figures 5 to 10 illustrate the model's predictions for the incremental coefficients ${d_{33}}^H$ and ${\mu_{33\mathrm{r}}}^T = {\mu_{33}}^T/\mu_o$ as well as ${d_{15}}^H$ for both Galfenol and Terfenol-D. The values are consistent with those found in the literature [38-39]. These results illustrate the model's ability to capture the behavior of these coefficients. This consistency with prior research findings reinforces the accuracy of the model's predictions, highlighting its potential as a valuable tool for analyzing and understanding the piezomagnetic behavior of Galfenol and Terfenol-D.

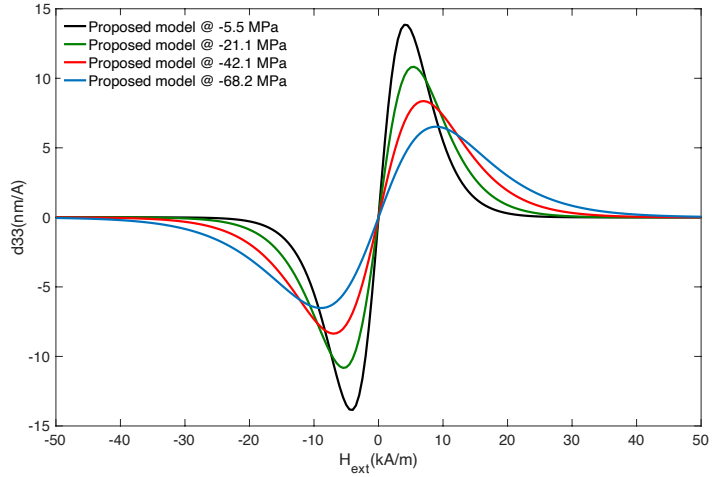

Figure 5: Prediction of incremental coefficient ${d_{33}}^{H}$ @ T_o =- 50 MPa with κ =-898640, τ =0.8415, η= -1.1555e-04and under different applied stresses [30] for the Galfenol

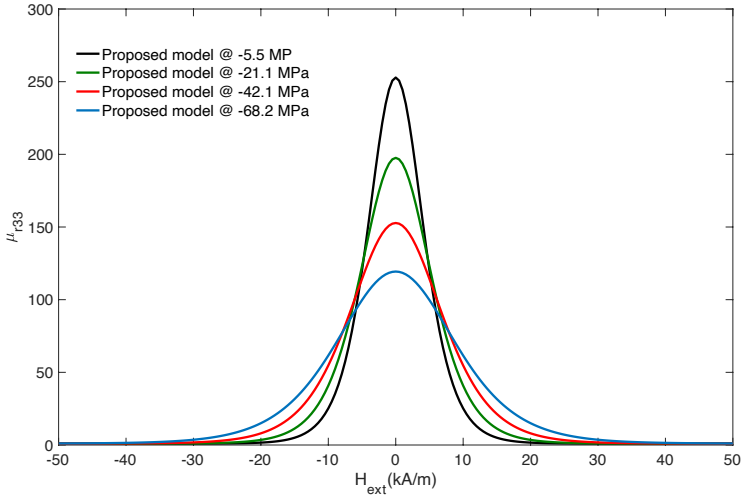

Figure 6: Prediction of incremental coefficient ${\mu_{\mathrm{r33}}}^{T}$ @ T_o =- 50 MPa with κ =-898640, τ =0.8415, η= -1.1555e-04 and under different applied stresses [30] for the Galfenol

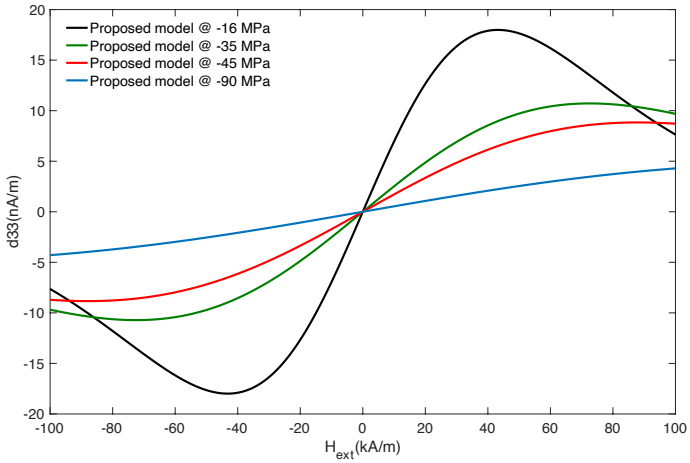

Figure 7: Prediction of incremental coefficients ${d_{33}}^{H}$ @ T_o =- 50 MPa with $\kappa = 0$, τ =0, η= -0.0020and under different applied stresses [37] for the Tefernol-D

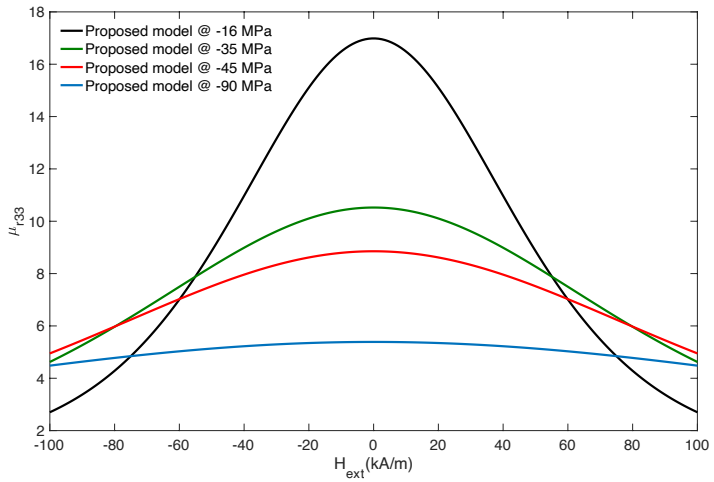

Figure 8: Prediction of incremental coefficient ${\mu_{r33}}^{T}$@ T_o =- 50 MPa with $\kappa = 0$, τ =0, η= -0.0020and under different applied stresses [37] for the Tefernol-D

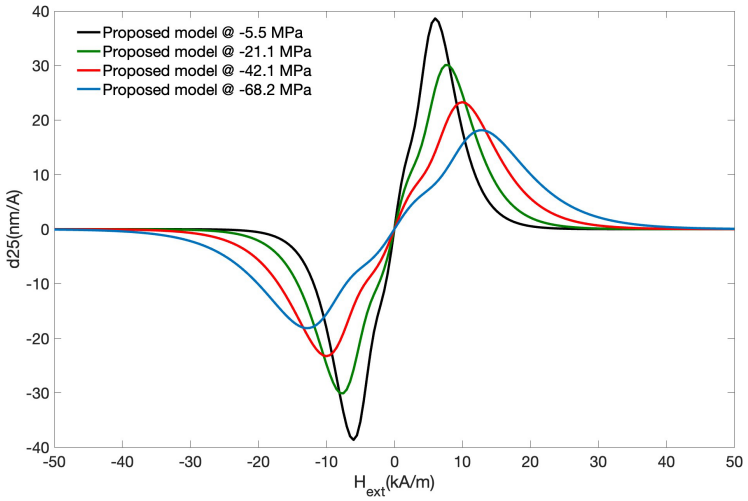

Figure 9: Prediction of incremental coefficients $d_{15}{}^{H}$ @ T_o =- 50 MPa with κ =-898640, τ =0.8415, η= -1.1555e-04 and under different applied stresses [30] for the Galfenol

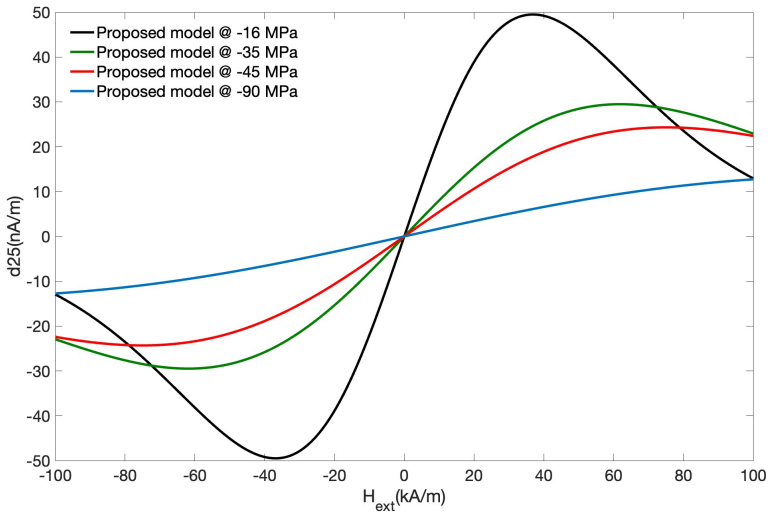

Figure 10: Prediction of incremental coefficients $d_{15}{}^{H}$ @ T_o =- 12 MPa with $\kappa = 0$, τ =0, η= -0.0020 and under different applied stresses [37] for the Terfenol-D

III. Finite Element Formulation

The finite element formulation of MECs coupled problem is derived by combining the equilibrium equations of elasticity (Newton's laws), magnetism (Ampère's law), and electricity (Gauss's law).

$$\mathrm{div}\boldsymbol{T} + \boldsymbol{f} = \rho_v \partial_t^2 \boldsymbol{u} \tag{19}$$

$$\mathrm{curl}\ \boldsymbol{H} = \boldsymbol{J} \tag{20}$$

$$\mathrm{div}\ \boldsymbol{D} = \rho \tag{21}$$

where $\boldsymbol{T}$ (N/m^2) represents the mechanical stress tensor, $\boldsymbol{u}$ the mechanical displacement, ρ_v the mass density of the material, $\boldsymbol{f}$ (N/m^3) the external applied volume force, $\boldsymbol{H}$ (A/m) denotes the magnetic field, $\boldsymbol{J}$ (A/m^2) represents the current density, $\boldsymbol{D}$ (C/m^2) represents the displacement field, and ρ (C/m^3) is volume density of the free electric charge. In our case, the source terms $(\boldsymbol{f}, \rho)$ set to zero due to the absence of external applied volume force, and the piezoelectric layer is treated as a perfect dielectric without any free electric charge.

The constitutive relations under the small signal linear approximation are a combination of the magneto-elastic and electro-elastic constitutive laws:

$$\boldsymbol{T} = c^{E,B}\boldsymbol{:S} - e^t\boldsymbol{E} - h^t\boldsymbol{B} \tag{22}$$

$$\boldsymbol{H} = v^S\boldsymbol{B} - h\boldsymbol{S} \tag{23}$$

$$\boldsymbol{D} = \varepsilon^S\boldsymbol{E} - e\boldsymbol{S} \tag{24}$$

where $\boldsymbol{S}$(-) denotes the mechanical strain, $\boldsymbol{E}$(V/m) represents the electric field, v^S (m/H) and ε^S (F/m) are the reluctivity and permittivity tensors under strain $\boldsymbol{S}$ constant, respectively. The coefficients h (A/m) and e (C/m^2) represent the incremental piezomagnetic and piezoelectric tensors around the bias point. The tensors c^E and c^B correspond to the piezoelectric and magnetostrictive elastic stiffness constants under constant electric field, $\boldsymbol{E}$, and magnetic field, $\boldsymbol{B}$, respectively. The symbol $()^t$ signifies the transpose operator.

It is important to note that, ${h_{ij}}^H = {q_{ij}}^H {v_{ij}}^S$, and $c^B_{ijkl} = c^H_{ijkl} + \left({q_{ij}}^H\right)^t {\nu_{\mathrm{ij}}}^S {q_{ij}}^H$, where ${q_{ij}}^H = c^H_{ijkl}{d_{ij}}^H$ is the piezomagnetic (N/Am) tensor coefficients and c^H is the magnetostrictive elastic stiffness constant material tensor under constant magnetic field, $\boldsymbol{H}$. The matrices and tensors involved in these relations can be found in Appendix C and the coefficients ${d_{ij}}^H$ and ${\nu_{\mathrm{ij}}}^S = \left({\mu_{\mathrm{ij}}}^S\right)^{-1}$ are extracted from the nonlinear model as proposed in section II.

The incremental coefficients are derived through the utilization of the nonlinear model outlined in the preceding section B. Integrating them into the FEM process is achieved through a nonlinear piecewise linear procedure.

By substituting equations (22),(23),(24) into equations (19), (20) and (21) , the resulting system of equations is as follows:

$$\mathrm{div}\left(c^{E,B}\boldsymbol{:S} - e^t\boldsymbol{E} - h^t\boldsymbol{B}\right) - \rho_v\partial_t^2\boldsymbol{u} = \boldsymbol{0} \tag{25}$$

$$\mathrm{curl}(v^S\boldsymbol{B} - h\boldsymbol{S}) = \boldsymbol{J} \tag{26}$$

$$\mathrm{div}\left(\varepsilon^S\boldsymbol{E} - e\boldsymbol{S}\right) = 0 \tag{27}$$

In the static regime, the current term $\boldsymbol{J}$ corresponds to the current source $\boldsymbol{J_s}$. However, in the harmonic regime, it is a combination of the eddy current $\boldsymbol{J_e}$ and the current source $\boldsymbol{J_s}$, with $\boldsymbol{J_e}$ expressed as follows:

$$\boldsymbol{J_e} = -\sigma(\partial\boldsymbol{A}/\partial t + \mathrm{grad}\emptyset_m) \tag{28}$$

where σ (S/m) is the electrical conductivity, $\boldsymbol{A}$ (Wb/m) the magnetic vector potential and $\emptyset_m(V)$ is an electric scalar potential.

For the axisymmetric case in cylindrical coordinates $\{e_r, e_\varphi, e_z\}$, only the φ components in the magnetic problem need to be considered. Consequently, the electric potential variable $\emptyset_m$ disappears, and in the

harmonic regime, the current density is expressed as $\boldsymbol{J_e} = -\sigma\, \partial \boldsymbol{A}/\partial t = j\omega\sigma \boldsymbol{A}$ [38]. In the mechanical problem, the symmetry about the z-axis implies that the stresses are independent of the φ resulting in all derivatives with respect to φ vanishing.

The finite element formulation is performed in employing the weighted residuals method:

$$\int_\Omega w_1.(\mathrm{div}(c^{E,B}\!:\boldsymbol{S} - e^t\boldsymbol{E} - h^t\boldsymbol{B}) + j\omega^2\rho_v\boldsymbol{u})d\Omega = 0 \quad (29)$$

$$\int_\Omega w_2.(\mathrm{curl}(\nu\mathrm{curl}\mathbf{A}) + \mathrm{curl}(-h\boldsymbol{S}) - j\omega\sigma\boldsymbol{A})d\Omega = 0 \quad (30)$$

$$\int_\Omega w_3.\mathrm{div}(-\boldsymbol{\varepsilon}\mathrm{grad}\emptyset - e\boldsymbol{S})d\Omega = 0 \quad (31)$$

where $w_{i=1,2,3}$ are the associated test functions and Ω is the problem domain.

Here, the unknown variables of the 2D axisymmetric coupled problem are:

- The new variable $\bar{A} = rA_\varphi$ component of $\boldsymbol{A}$
- The radial u_r (r direction) and axial u_z (z direction) components of the displacement $\boldsymbol{u}$.
- The electric scalar potential ∅ due to piezoelectric effect according to the r and z directions.

The fields $\boldsymbol{S}$, $\boldsymbol{E}$ and $\boldsymbol{B}$ can be expressed in terms of the state variables with the mechanical displacement $\boldsymbol{u}$, the magnetic vector potential $\bar{A}$ and the electric scalar potential ∅.

In 2D coordinates, the relations are given by:

The strain $\boldsymbol{S} = \mathfrak{D}\boldsymbol{u}$ in the mechanical domain is given by:

$$\boldsymbol{S} = \begin{Bmatrix} S_r \\ S_\varphi \\ S_z \\ S_{rz} \end{Bmatrix} = \mathfrak{D}\boldsymbol{u} = \begin{bmatrix} \partial/\partial r & 0 \\ 1/r & 0 \\ 0 & \partial/\partial z \\ \partial/\partial z & \partial/\partial r \end{bmatrix} \begin{Bmatrix} u_r \\ u_z \end{Bmatrix} = G_u(\boldsymbol{u}) \quad (32)$$

where $G_u = \mathfrak{D} = \mathrm{sym}(\mathrm{grad}) = \frac{1}{2}\left(\mathrm{grad} + \mathrm{grad}^{\mathrm{t}}\right)$.

The magnetic induction $\boldsymbol{B} = \mathrm{curl}(\boldsymbol{A})$ in the magnetic domain is given by:

$$\boldsymbol{B} = \xi\mathrm{grad}\, A_\varphi = \frac{1}{r}\xi\mathrm{grad}\, \bar{A} = \begin{Bmatrix} \boldsymbol{B_r} \\ \boldsymbol{B_z} \end{Bmatrix} = \frac{1}{r}\begin{Bmatrix} -\frac{\partial \bar{A}}{\partial z} \\ \frac{\partial \bar{A}}{\partial r} \end{Bmatrix} = \frac{1}{r}G_A\left(\bar{A}\right) \quad (33)$$

where $G_{\bar{A}} = \xi\mathrm{grad},\ \text{with}\ \xi = [0 \quad 1, -1 \quad 0]^T$ represents a rotation matrix in cylindrical coordinates.

The electric field $\boldsymbol{E} = -\mathrm{grad}\emptyset$ in the piezoelectric domain is given by:

$$\boldsymbol{E} = \begin{Bmatrix} \boldsymbol{E_r} \\ \boldsymbol{E_z} \end{Bmatrix} = -\begin{Bmatrix} \frac{\partial \emptyset}{\partial r} \\ \frac{\partial \emptyset}{\partial z} \end{Bmatrix} = G_\emptyset(\emptyset) \quad (34)$$

where $G_\emptyset = -\mathrm{grad}$

After applying the classical mechanical, magnetic and electrical Neumann conditions $\int_{\partial\Omega} w.n.\boldsymbol{T}\, d\Gamma = 0$,

$\int_{\partial\Omega} w.n \wedge \mathrm{H}\, d\Gamma = 0, \int_{\partial\Omega} \mathrm{w}.\boldsymbol{\varepsilon}\frac{\partial \emptyset}{\partial n} d\Gamma = 0$, in each boundary domain $\partial\Omega$ problem, the general finite element formulation derived from equations (22-a-b-c) is simplified as:,

$$\int_{\Omega} \left(\mathfrak{D}w_1 : c^{E,B} : \mathfrak{D}\boldsymbol{u} + \mathfrak{D}w_1 : e^t \mathrm{grad}(\emptyset) - \mathfrak{D}w_1 : \frac{h^t}{r}\, \mathrm{curl}(\boldsymbol{A}) - j\omega^2 w_1 \rho_v \boldsymbol{u}\right) d\Omega = 0 \quad (35)$$

$$\int_{\Omega} \left(\mathrm{curl}(w_2).\frac{v^S}{r}.\mathrm{curl}(\boldsymbol{A}) - \mathrm{curl}(w_2).h.\mathfrak{D}\boldsymbol{u} - j\omega w_2.\frac{\sigma}{r}.\boldsymbol{A}\right) d\Omega = 0 \quad (36)$$

$$\int_{\Omega} (\mathrm{grad}\emptyset.\varepsilon^S \mathrm{grad}(w_3) + \mathfrak{D}\boldsymbol{u} e \mathrm{grad}(w_3))\ d\Omega = 0 \quad (37)$$

When employing the Galerkin approach, namely $w_1 = u^*$, $w_2 = rA_\varphi{}^* = \bar{A}^*$ and $w_3 = \emptyset^*$, along with the 2D relations (35), (36), and (37), we obtain finally:

$$\int_{\Omega} \left(G_{u^*}\, \boldsymbol{u}^* c^{E,B} G_u \boldsymbol{u} + G_u\, \boldsymbol{u}^* e^t G_\emptyset \emptyset - G_u\, \boldsymbol{u}^* \frac{h^t}{r}\, G_{\bar{A}} \bar{A} + j\omega^2 \boldsymbol{u}^* \rho_v \boldsymbol{u}\right) d\Omega = 0 \quad (38)$$

$$\int_{\Omega} \left(.\, G_{\bar{A}} \bar{A}^*.\frac{v^S}{r^2}.G_{\bar{A}}\bar{A} - G_{\bar{A}}\bar{A}^*.\frac{h}{r}.G_u \boldsymbol{u} - j\omega \bar{A}^*.\frac{\sigma}{r^2}\bar{A}\right) d\Omega = 0 \quad (39)$$

$$\int_{\Omega} (G_\emptyset \emptyset^*.\varepsilon^S.G_\emptyset \emptyset + G_{\emptyset^*}\emptyset^*.e.G_u \boldsymbol{u}) d\Omega = 0 \quad (40)$$

A remark regarding formulation (26-e). In the case of a magnetic-only problem, the choice of the test function would have been $w_2 = \bar{A}^*$ (not $rA_\varphi{}^*$) with $G_{\bar{A}^*} = \xi \mathrm{grad}\,\bar{A} = r.G_{\bar{A}}$, leading to the well-known following formulation $\int_{\Omega} \left(.\, G_{\bar{A}} \bar{A}^*.\frac{v^S}{r}.G_{\bar{A}}\bar{A} - j\omega \bar{A}^*.\frac{\sigma}{r}\bar{A}\right) d\Omega = 0$ [40]. In the context of a magnetoelectric problem, it is crucial to maintain symmetry in the expression of the magneto-elastic and elasto-electric coupling matrices. As for the expression of the elasto-electric coupling, symmetry is preserved (38) and (40), namely $G_{\emptyset^*}\emptyset^*.e.G_u \boldsymbol{u} = sym(G_u\, \boldsymbol{u}^* e^t G_\emptyset \emptyset)$; however, to maintain that of the magneto-elastic coupling $G_{\bar{A}}\bar{A}^*.\frac{h}{r}.G_u \boldsymbol{u} = sym\left(G_u\, \boldsymbol{u}^* \frac{h^t}{r}\, G_{\bar{A}}\bar{A}\right)$ between (38) and (39), it is essential to use the test function $w_2 = rA_\varphi{}^* = \bar{A}^*$.

A. Boundary conditions

The elastic, electric and magnetic boundary conditions of the solution domain associated in the resolution of the system in 2D axisymmetric are, respectively, illustrated in Figure 11.
Let, Ω_u, $\Omega_\emptyset$and Ω_A denote the mechanical, the electrical and magnetic domains respectively, with boundaries denoted as Γ_δ, $\Gamma_\emptyset$ and Γ_A. The Dirichlet boundary condition for the electrical field is given by:

$$\emptyset = 0 \text{ on } \Gamma_\emptyset \quad (41)$$

In the magnetic problem, the external magnetic source $\boldsymbol{J_s}$ is implicitly incorporated by imposing the following Dirichlet conditions at Ω_A [42-43]:

$$\bar{A} = 0 \text{ on } \Gamma_A(r = 0) \text{ and } \bar{A} = \mathrm{a}_o \text{ on } \Gamma_A(r = r_{max}) \quad (42)$$

As a result, by imposing these Dirichlet conditions, a uniform axial magnetic flux $\mathbf{B_o}$ (depicted by green arrows in Figure 11) is guaranteed along the transverse direction z of the composite, serving as the magnetic source. In a 2D context, the magnetic flux is defined as $a_0 = B_0 \Delta_z$ with $\Delta_r = (r_{max} - r_{min})$. Consequently, the small signal field h_{ac} or the static bias H_{dc} is defined as:

$$h_{ac}\, or\, H_{dc} = B_0/\mu_0 = a_0/(\Delta_r \mu_0) \quad (43)$$

For example, in considering $h_{ac} = 79.57$ kA/m, i.e. 1 Oe, it is necessary to impose $a_0 = 1.6$ Wb/m.

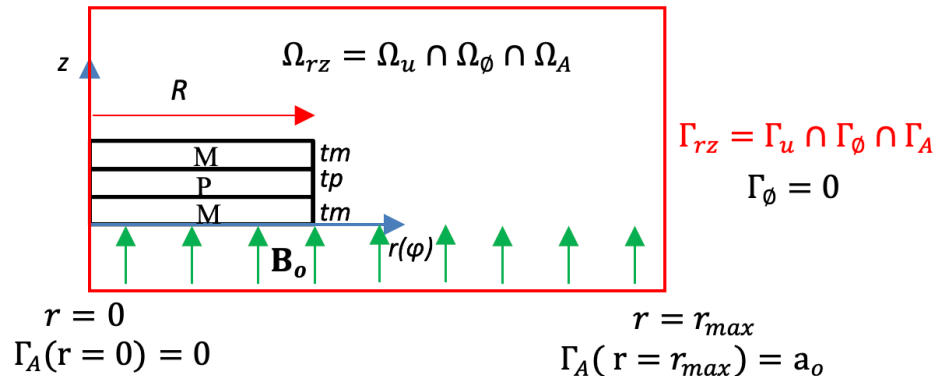

Figure 11: Illustration of the magnetic, electric, and elastic boundary conditions

B. Discretization procedure

In this proposed FEM analysis, the linear triangular element <*ijm*> is utilized for nodal discretization of all fields. The shape functions for this element are defined as follows:

$$N_u = \begin{bmatrix} N_i & 0 & N_j & 0 & N_m & 0 \\ 0 & N_i & 0 & N_j & 0 & N_m \end{bmatrix} \quad (44\text{-a})$$

$$N_{A,\emptyset} = N = [N_i \quad N_j \quad N_m] \quad (44\text{-b})$$

where $N_{k=i,j,m} = \frac{1}{2\Delta}(\alpha_k + \beta_k r + \gamma_k z)$. Here, Δ represents the cross-sectional area of a triangular element. Expressions of descriptions of α_k, β_k and γ_k are given in Appendix D.

The unknown variables of the problem are discretized using nodal degrees of freedom (DoF), represented as $A_e = N_k \bar{A}$, $\boldsymbol{u_e} = N_k \boldsymbol{u}$ and $\emptyset_e = N_k \emptyset$, where A_e, $\boldsymbol{u_e}$ and $\emptyset_e$ are unknown variables in each finite element. Following the finite element discretization of the weak forms (38),(39) and (40), the resulting system equation in the harmonic regime ($\partial/\partial t \to j\omega$) is given by:

$$\partial_t^2[M]\{X\} + \partial_t[C]\{X\} + [K]\{X\} = \{F\} \quad (45)$$

$$[K - \omega^2 M + j\omega C]\{X\} = \{F\} \quad (46)$$

with $[K] = \begin{bmatrix} K_{uu} & K_{u\emptyset} & K_{uA} \\ {K_{u\emptyset}}^t & -K_{\emptyset\emptyset} & 0 \\ {K_{uA}}^t & 0 & K_{AA} \end{bmatrix}$, $[M] = \begin{bmatrix} M_{uu} & 0 & 0 \\ 0 & 0 & 0 \\ 0 & 0 & 0 \end{bmatrix}$, $[C] = \begin{bmatrix} C_{uu} & 0 & 0 \\ 0 & 0 & 0 \\ 0 & 0 & C_{AA} \end{bmatrix}$, $\{X\} = \begin{Bmatrix} \boldsymbol{u_e} \\ \emptyset_e \\ A_e \end{Bmatrix}$ and $\{F\} = \begin{Bmatrix} 0 \\ 0 \\ a_o \end{Bmatrix}$

in reduced form:

$$\begin{bmatrix} \mathcal{K}_{uu} & K_{u\emptyset} & K_{uA} \\ {K_{u\emptyset}}^t & -K_{\emptyset\emptyset} & 0 \\ {K_{uA}}^t & 0 & \mathcal{K}_{AA} \end{bmatrix} \begin{Bmatrix} \boldsymbol{u_e} \\ \emptyset_e \\ \mathrm{A_e} \end{Bmatrix} = \begin{Bmatrix} 0 \\ 0 \\ a_o \end{Bmatrix} \tag{47}$$

where, in static regime ($\partial/\partial t = 0$) $\mathcal{K}_{uu} = K_{uu}$, $\mathcal{K}_{AA} = K_{AA}$ and a_o impose the static bias $\boldsymbol{H}_{dc}$ magnetic field, whereas in dynamic regime $\mathcal{K}_{uu} = K_{uu} + j\omega C_{uu} - \omega^2 M_{uu}$, $\mathcal{K}_{AA} = K_{AA} + j\omega C_{AA}$ and a_o impose the small harmonic $\boldsymbol{h}_{ac}$.

Here, the resolution is carried out using the centroidal point method [41] defined by $(\bar{r}, \bar{z})$, where $\bar{r} = \frac{r_i + r_j + r_m}{3}$ and $\bar{z} = \frac{z_i + z_j + z_m}{3}$. By employing this method, the integral domain is transformed to $\int_\Omega \mathrm{d}\Omega = 2\pi \int_\Delta \bar{r}\mathrm{drdz}$. The expressions of $G_A = \xi\mathrm{grad}[N_k]$, $G_u = \mathrm{sym}(\mathrm{grad}[N_k])$, and $G_\emptyset = \mathrm{grad}[N_k]$ are given in Appendix E.

In this way, the sub-matrices are defined as:

$$[K_{mm}] = \sum_e 2\pi \int_\Omega [G_m]^t [\Lambda] [G_m] \bar{r} d\mathrm{rdz}, \ \Lambda = \begin{cases} c^{E,B} & \text{if } m = \boldsymbol{u} \\ \varepsilon^S & \text{if } m = \emptyset \\ v^S/r & \text{if } m = A \end{cases} \tag{48}$$

$$[K_{mn}] = \sum_e 2\pi \int_\Omega [G_i]^t [\Theta]^t [G_j] \bar{r} d\mathrm{rdz}, \ \Theta = \begin{cases} \mathrm{e} & \text{if } m = \boldsymbol{u}, n = \emptyset \\ h & \text{if } m = \boldsymbol{u}, n = A \end{cases} \tag{49}$$

$$[M_{uu}] = \sum_e 2\pi \int_\Omega [N_u]^t \rho_m [N_u] \bar{r} d\mathrm{rdz} \tag{50}$$

$$[C_{uu}] = 2\varsigma [M_{uu}] \omega_n = \alpha [M_{uu}] + \beta [K_{uu}] \tag{51}$$

$$[C_{AA}] = \sum_e 2\pi \int_\Omega \left(\frac{\sigma}{\bar{r}}\right) [N]^t [N] \bar{r} d\mathrm{rdz} = \sum_e 2\pi \int_\Omega \sigma [N]^t [N] d\mathrm{rdz} \tag{52}$$

C_{AA} denotes the eddy current losses, and C_{uu} is the mechanical damping matrix, where ς is a modal damping parameter, and $\omega_n = K_{uu}/M_{uu}$ is the natural angular frequency. The parameter ς can be represented by the Rayleigh damping coefficients α and β, given as $\varsigma = \frac{\alpha}{2\omega_n} + \frac{\beta\omega_n}{2}$. The α and β multiplier terms lack physical significance; they are simply required to define a general damping proportional to the linear combination of the mass and stiffness matrices.

Typically, in a mechanical oscillation system, for weak to moderate Rayleigh damping the parameter ς is correlated with the mechanical quality factor Q_{mech}, expressed as:

$$Q_{mech} = 1/(2\,\varsigma) \tag{53}$$

The value of Q_{mech} cannot be directly calculated; instead, it needs to be measured at resonance using the formula $Q_{mech} = \frac{\omega_r}{\Delta_\omega}$. Here, $\omega_r = \omega_n\sqrt{1 - \varsigma^2}$ is the angular frequency resonance and Δ_ω represents the bandwidth of the amplitude resonance of the magnetoelectric coefficient $\tilde{\alpha}_V = \delta V/\delta h_{ac}$ measured at $1/\sqrt{2}$ of its peak.

As mentioned in [44], typically in piezoelectric transducer vibration occurs the viscous damping, namely

$\alpha = 0$. This assumption holds true for a magnetoelectric composite. In this context:

$$\beta = \frac{1}{Q_{mech}\omega_r} \tag{54}$$

C. Electrodes effect and impedance load implementation

The formulation has incorporated distinct degrees of freedom (DoFs) for the upper and lower electrodes of the piezoelectric layer. This inclusion guarantees a clear equipotential connection at both the top and bottom of the layer, ensuring continuity for the unknown electric scalar potential $\emptyset$.

In the harmonic regime, an electrical load impedance Z can be introduced to simulate the input impedance of an electronic device connected between the electrodes. This impedance can be integrated into the solution system through the application of Ohm's law:

$$\phi K_{\phi Q} - \bar{Z} I = 0 \tag{55}$$

where $I = \frac{dQ}{dt} = j\omega Q$ and $\bar{Z} = 2\pi Z$ is the reduced impedance to consider the transformation domain $\int_\Omega \mathrm{d}\Omega = 2\pi \int_\Delta \bar{r}\mathrm{d}r\mathrm{d}z$.

where Q represents the total electrical charge across the electrodes and becomes an additional unknown in the resolution system. $K_{\phi Q}$ is an incidence matrix where the elements are set to 1 or -1 depending on whether the related node is associated with the top electrode or the bottom electrode, while the remaining elements are set to 0 [43].

The matrix elements of the final system in harmonic regime (30) are:

$$[M] = \begin{bmatrix} M_{uu} & 0 & 0 & 0 \\ 0 & 0 & 0 & 0 \\ 0 & 0 & 0 & 0 \\ 0 & 0 & 0 & 0 \end{bmatrix}, [C] = \begin{bmatrix} C_{uu} & 0 & 0 & 0 \\ 0 & 0 & 0 & 0 \\ 0 & 0 & \bar{Z} & 0 \\ 0 & 0 & 0 & C_{AA} \end{bmatrix}, [K] = \begin{bmatrix} K_{uu} & K_{up} & 0 & K_{ua} \\ K_{up}^t & K_{pp} & K_{pq} & 0 \\ K_{ua}^t & K_{qp} & 0 & 0 \\ & 0 & 0 & K_{aa} \end{bmatrix} \{X\} = \begin{bmatrix} \boldsymbol{u_e} \\ \emptyset_e \\ Q \\ \mathrm{A}_e \end{bmatrix}, \{F\} = \begin{bmatrix} 0 \\ 0 \\ 0 \\ a_0 \end{bmatrix} \tag{56}$$

In reduced form:

$$\begin{bmatrix} \mathcal{K}_{uu} & K_{up} & 0 & K_{ua} \\ K_{up}^t & K_{pp} & K_{pq} & 0 \\ K_{ua}^t & K_{qp} & -j\bar{Z}\omega & 0 \\ & 0 & 0 & \mathcal{K}_{aa} \end{bmatrix} \begin{bmatrix} \boldsymbol{u_e} \\ \emptyset_e \\ Q \\ \mathrm{A}_e \end{bmatrix} = \begin{bmatrix} 0 \\ 0 \\ 0 \\ a_0 \end{bmatrix} \tag{57}$$

D. The nonlinear static piecewise procedure

The piecewise nonlinear process is applied in the static regime under a bias point (H_o, T_o), leveraging the proposed nonlinear model outlined in the preceding sections A and B. The steps of the piecewise linear solution are outlined in Figure 11 and can be summarized as follows:

Initially, the nonlinear model is employed to determine the incremental coefficients ${q_{ij}}^H$, ${\nu_{\mathrm{ij}}}^S$ and ${c_{\mathrm{ijkl}}}^B$ for each finite element of the magnetostrictive material. Following this, the incremental magnetostrictive constitutive equations are systematically solved using the Jacobian matrix jac under the bias point (H_o, T_o) [12].

$$jac = \begin{bmatrix} c^B = \frac{\partial \boldsymbol{T}}{\partial \boldsymbol{S}}\Big|_{(H_o,T_o)} & -h = \frac{\partial \boldsymbol{T}}{\partial \boldsymbol{B}}\Big|_{(H_o,T_o)} \\ -h^t = \frac{\partial \boldsymbol{H}}{\partial \boldsymbol{S}}\Big|_{(H_o,T_o)} & v^S = \frac{\partial \boldsymbol{H}}{\partial \boldsymbol{B}}\Big|_{(H_o,T_o)} \end{bmatrix} \tag{58}$$

After that, the system in static regime ($\partial_t = 0$) the magnetoelectric problem $[K]\{X\} = \{F\}$ can be solved such as:

$$\begin{bmatrix} \mathrm{K}_{uu} & K_{u\emptyset} & K_{uA} \\ K_{u\emptyset}{}^t & -K_{\emptyset\emptyset} & 0 \\ K_{uA}{}^t & 0 & \mathrm{K}_{AA} \end{bmatrix} \begin{Bmatrix} \boldsymbol{u_e} \\ \emptyset_e \\ \mathrm{A}_e \end{Bmatrix} = \begin{Bmatrix} 0 \\ 0 \\ a_o \end{Bmatrix} \tag{59}$$

Finally, the incremental solutions ΔS and ΔB, obtained from equations (23) and (24), are utilized to update the incremental set bias points ($\Delta\boldsymbol{H}$, $\Delta\boldsymbol{T}$) as follows:

$$\begin{bmatrix} \Delta\boldsymbol{T} \\ \Delta\boldsymbol{H} \end{bmatrix} = jac \begin{bmatrix} \Delta\boldsymbol{S} \\ \Delta\boldsymbol{B} \end{bmatrix} = \begin{bmatrix} c^B & -h \\ -h^t & v^S \end{bmatrix} \begin{bmatrix} \Delta\boldsymbol{S} \\ \Delta\boldsymbol{B} \end{bmatrix} \tag{60}$$

The process is iterated until the maximum step condition is reached. At the end of the process, the obtained incremental coefficients at the desired excitation static magnetic bias point $\boldsymbol{H}_{dc}$ are stored and utilized for harmonic analysis.

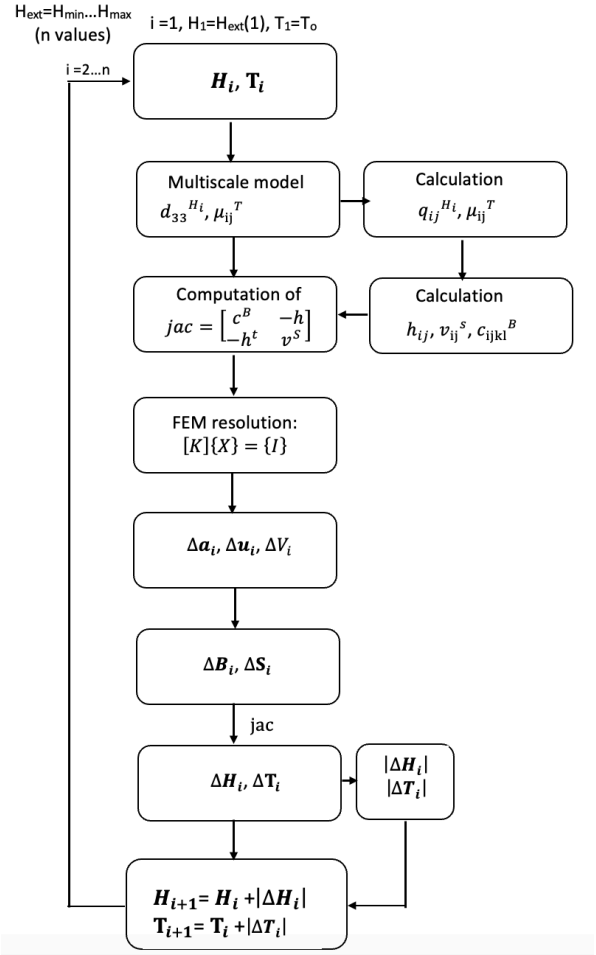

Figure 11: Flowchart of piecewise linear solution process to compute the magnetostrictive coefficient for simulation of magnetoelectric material.

IV. NUMERICAL EXAMPLES

This section presents two numerical examples comparing the proposed FEM multiphysics model (solid lines) implemented with Matlab® with measurement data (dotted lines) obtained from MEC disks in TT mode, as documented in the literature [7], [9-10]. The first numerical example centers on a Galfenol/BTO/Galfenol composite disk, as outlined in [9-10]. This disk features a 1mm thickness for each layer, with Galfenol having a 6mm radius and BTO a 5mm radius. Detailed material properties and parameter values are available in Appendix F. The meshing and the field distributions are given in Figure 12.

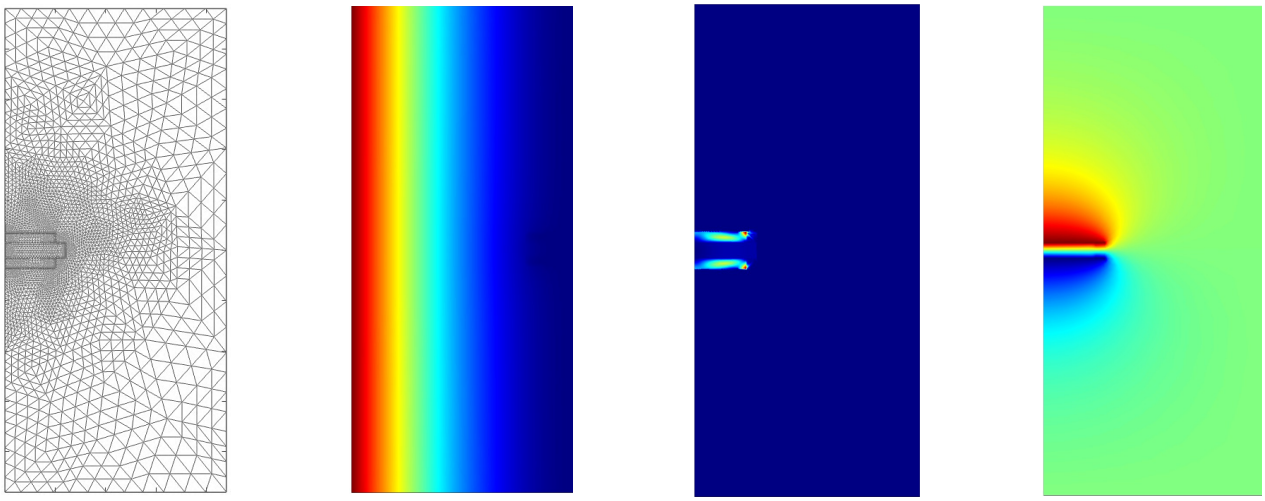

Meshing, 3214 finite elements | The magnetic potential A source | The magnitude of the induced displacement inside the composite $\boldsymbol{u}$ | The induced electric scalar potential $\emptyset$

Figure 12: Illustration of the meshing of problem and field distributions from simulation results

Figures 13 and 14 show the comparison between simulation results and measurements for the Galfenol/BTO/Galfenol disk. In Figure 13, simulation results are attained by assuming identical incremental coefficient values for each finite element that is a common a regrettably practice in the literature. In Figure 14, the incremental coefficients are calculated using the nonlinear piecewise procedure, guaranteeing accurate values through an adequate number of iterations. It is evident that both cases exhibit strong agreement between simulations and measurements. Nevertheless, the results obtained through the piecewise nonlinear procedure provide a more accurate consideration of folding effects namely the edge effects on the structure. This underscores the significance of employing a nonlinear approach to effectively capture the non-uniform distribution of incremental coefficients within the material.

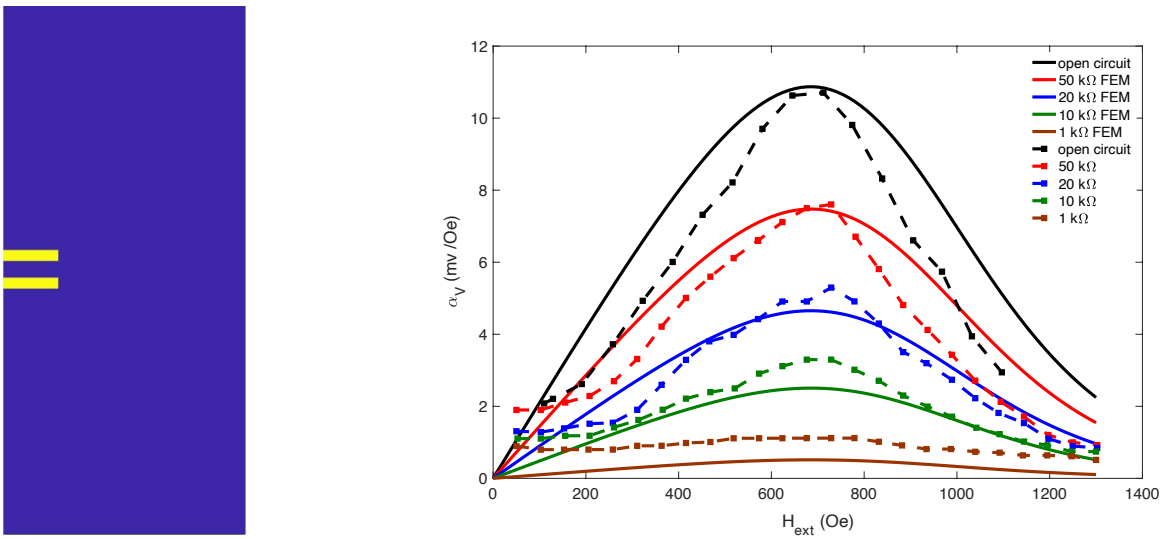

13: (a) Uniform distribution of an incremental coefficient q_{33} values for each finite element, (b) A Magnetoelectric voltage of Galfenol/BTO/Galfenol ME disk as a function of the static bias $\boldsymbol{H}_{dc}$under various electrical resistance load values for $\boldsymbol{h}_{ac}$ =1 Oe @ 1 kHz. Data measurement from [10] and FEM simulations are performed without the nonlinear piecewise procedure.

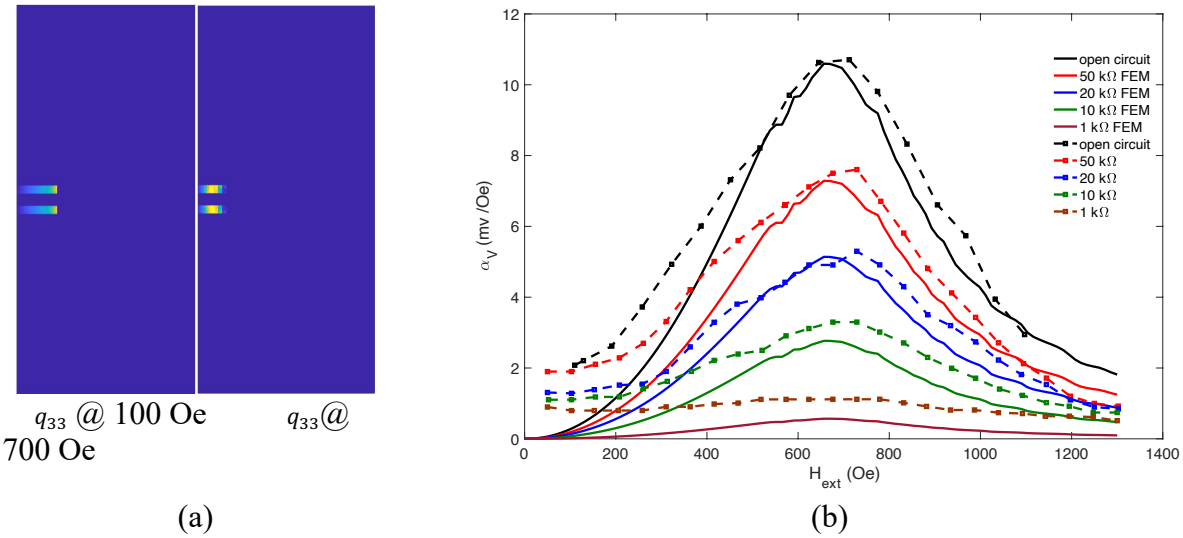

Figure 14: (a) Distributions of incremental coefficient q_{33} calculated with the nonlinear piecewise procedure in each finite element for both cases @ 100 Oe and 700 Oe, (b) Magnetoelectric voltage of Galfenol/BTO/Galfenol ME disk as a function of the static bias $\boldsymbol{H}_{dc}$under various electrical resistance load values for $\boldsymbol{h}_{ac}$ =1 Oe @ 1 kHz. Data measurement from [10] and FEM simulations are performed with the nonlinear piecewise procedure.

Figure 15 illustrates the frequency dependence of the ME voltage coefficient $\tilde{\alpha}_V$ for $\boldsymbol{h}_{ac}$ =1 Oe under $\boldsymbol{H}_{dc}$=1000 Oe. The solid lines represent the results obtained from the proposed FEM multiphysics model, while the dot lines represent the measurement data. Notably, a good agreement is observed between the simulation results and the measurements.

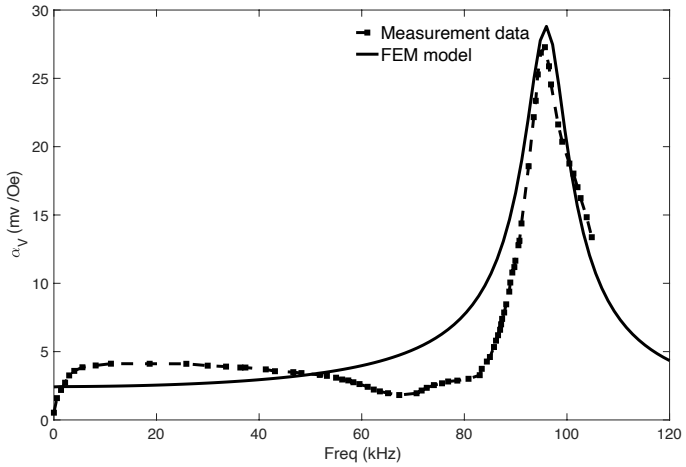

Figure 15: $\tilde{\alpha}_V$ in function of frequency. Data measurement from [9] and FEM simulations performed for $\boldsymbol{h}_{ac}$ =1 Oe under $\boldsymbol{H}_{dc}$=1000 Oe.

The second numerical example centers on the Terfenol-D/PZT/Terfenol-D composite disk discussed in [7]. In contrast to the first example, the radius of each layer sample is now equal, measuring 4 mm, while the thicknesses vary. The PZT layer has a thickness of 0.8 mm, and the Terfenol-D layer has the same thickness of 0.8 mm. For this example, the piecewise nonlinear procedure was employed, built upon the Terfenol-D model depicted in section C. Detailed material properties and parameter values can be found in Appendix F.

Figure 16 presents the frequency-dependent behavior of the ME electric coefficient $\tilde{\alpha}_E$ for $\boldsymbol{h}_{ac}$ =1 Oe under $\boldsymbol{H}_{dc}$=120 Oe. e. A comparison between the proposed FEM multiphysics model (solid lines) and the measurement data (dotted lines) from [7] reveals an excellent agreement.

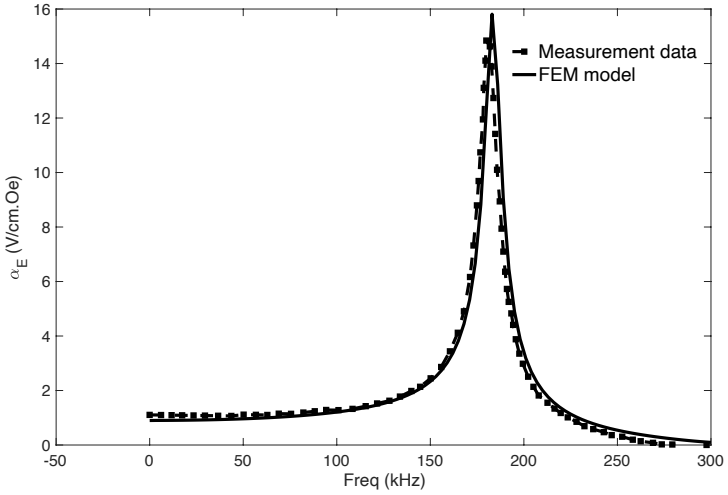

Figure 16: $\tilde{\alpha}_E$ in function of frequency. Data measurement from [7] and FEM simulations performed for $\boldsymbol{h}_{ac}$ =1 Oe under $\boldsymbol{H}_{dc}$=120 Oe.

Figures 17 and 18 illustrate the frequency-dependent behavior of the magnetoelectric coefficient $\tilde{\alpha}_E$ under various resistance load values and the accompanying shift in resonance frequency. The simulation results generated by our proposed FEM multiphysics model (solid lines) closely match the measurements [7], displaying a comparable trend as the electric load diminishes. This alignment underscores the importance of our model's conclusions, as impedance matching plays a pivotal role in the design and utilization of MECs devices.

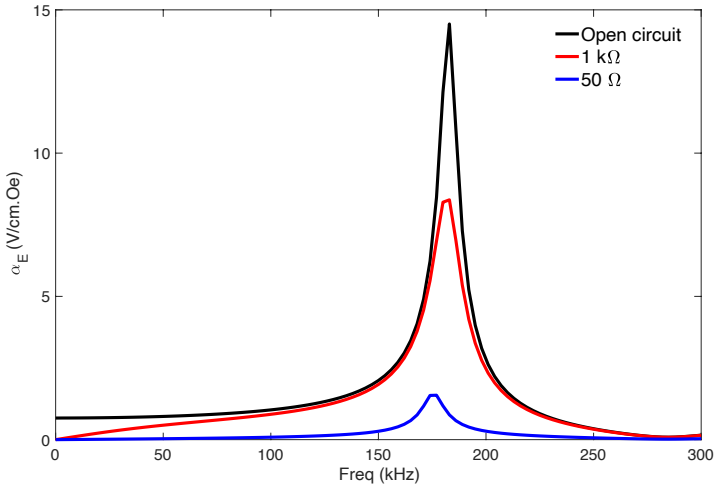

Figure 17: $\tilde{\alpha}_E$ in function of frequency under different resistive loads

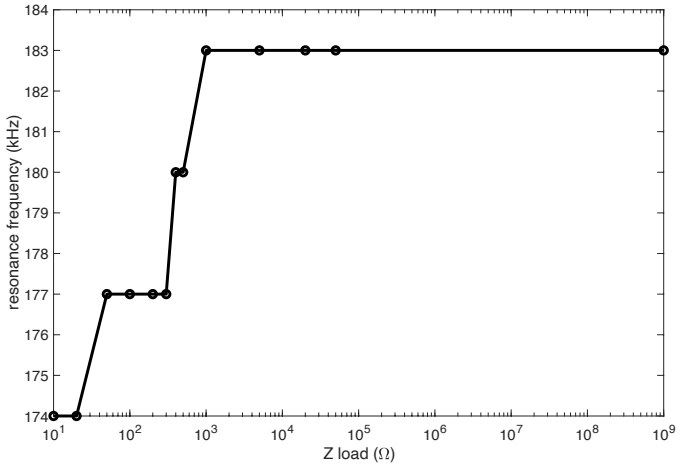

Figure 18: The resonance frequency under different resistive loads

V. Conclusion

This study introduced a 2D axisymmetric finite element multiphysics analysis to assess the performance of laminated ME disks. The analysis encompassed two key phases: a static magnetic biasing analysis that considered the non-linear behavior of the magnetostrictive material using a magneto-elastic approach, and a harmonic performance analysis built on the assumption of small signal behavior through a linear model. The numerical investigations of tri-layer laminated ME disks demonstrated strong agreement with experimental results. The 2D analysis emerged as a valuable tool for evaluating the performance of ME composite disks in the context of energy conversion.

Additionally, the study explored a nonlinear magnetostrictive model integrated with a 2D axisymmetric finite element method. It introduced a nonlinear piecewise process, which offers advantages in terms of computational efficiency and straightforward incorporation of nonlinearity. Future extensions of this research could encompass the application of the proposed solver to more extensive nonlinear multi-physics problems, the integration of parallel computing, and enhancements in computational efficiency and convergence rate.

REFERENCES

[1] Dong, Shuxiang, Jie-Fang Li, and Dwight Viehland. "Characterization of magnetoelectric laminate composites operated in longitudinal-transverse and transverse–transverse modes." Journal of Applied Physics 95.5 (2004): 2625-2630.

[2] Jia-Mian Hu and Ce-Wen Nan, "Opportunities and challenges for magnetoelectric devices", APL Mater. 7, 080905 (2019); doi: 10.1063/1.5112089

[3] Bichurin M, Petrov R, Sokolov O, Leontiev V, Kuts V, Kiselev D, Wang Y. Magnetoelectric Magnetic Field Sensors: A Review. *Sensors*. 2021; 21(18):6232. https://doi.org/10.3390/s21186232

[4] Orpita Saha *et al* 2022 *Smart Mater. Struct.* **31** 113001

[5] S. Kopyl, et al , Magnetoelectric effect: principles and applications in biology and medicine– a review, Materials Today Bio, Volume 12, 2021, 100149,ISSN 2590-0064.

[6] Lou, Guofeng, Xinjie Yu, and Shihua Lu. 2017. "Equivalent Circuit Model of Low-Frequency Magnetoelectric Effect in Disk-Type Terfenol-D/PZT Laminate Composites Considering a New Interface Coupling Factor" *Sensors* 17, no. 6: 1399. https://doi.org/10.3390/s17061399

[7] Ru Zhang, Gaojian Wu, Ning Zhang, Equivalent circuit method for resonant magnetoelectric effect in disk-shaped laminated composites, Eur. Phys. J. Appl. Phys. 69 (1) 10602 (2015), DOI: 10.1051/epjap/2014140421.

[8] Guoxi Liu, Chunli Zhang, Weiqiu Chen, and Shuxiang Dong , "Eddy-current effect on resonant magnetoelectric coupling in magnetostrictive-piezoelectric laminated composites", Journal of Applied Physics 114, 027010 (2013) https://doi.org/10.1063/1.4812218.

[9] Lei Wang, Zhaofu Du, Chongfei Fan, Lihong Xu, Hongping Zhang, Dongliang Zhao, Magnetoelectric properties of Fe–Ga/BaTiO3 laminate composites, Journal of Alloys and Compounds, Volume 509, Issue 2, 2011, Pages 508-511, ISSN 0925-8388.

[10] Lei Wang, Zhaofu Du, Chongfei Fan, Lihong Xu, Hongping Zhang, Dongliang Zhao, Effect of load resistance on magnetoelectric properties in FeGa/BaTiO3/FeGa laminate composites, Journal of Alloys and Compounds, Volume 509, Issue 30, 2011, Pages 7870-7873, ISSN 0925 8388,

[11] Zhaofu Du, Sam Zhang, Chunlin He, Hui Ding, Dongliang Zhao, Closed magnetic circuit FeGa/BaTiO3/FeGa sandwich structure for high magnetoelectric effect, Journal of Alloys and Compounds, Volume 587, 2014, Pages 688-691,ISSN 0925-8388,

[12] T. A. Do, H. Talleb, A. Gensbittel and Z. Ren, "3-D Finite Element Analysis of Magnetoelectric Composites Accounting for Material Nonlinearity and Eddy Currents," in IEEE Transactions on Magnetics, vol. 55, no. 10, pp. 1-8, Oct. 2019, Art no. 7402008, doi: 10.1109/TMAG.2019.2926237.

[13] Amritesh Kumar, A. Arockiarajan, " *Evolution of nonlinear magneto-elastic constitutive laws in ferromagnetic materials: A comprehensive review*" , Journal of Magnetism and Magnetic Materials,Volume 546,,2022,168821,ISSN 0304-8853,

[14] Hong Yao, Yang Shi, Yuan-Wen Gao, " A mechanical-thermo-magneto model for self-biased magnetoelectric effect in laminated composite", *Journal of Magnetism and Magnetic Materials*, vol. 401,2016, 1046-1053,ISSN 0304-8853,

[15] S. Chakrabarti, "Modeling of 3D Magnetostrictive Systems with Application to Galfenol and Terfenol-D Transducers," Ph.D. dissertation, Dept. Mech. Eng., Ohio State Univ., Columbus, OH, US, 2011.

[16] S. Chakrabarti and M. J. Dapino, "Fully coupled discrete energy-averaged model for Terfenol-D", Journal of Applied Physics 111, 054505 (2012).

[17] D. Armstrong William , "Magnetization and magnetostriction processes in Tb (0.27- 0.30) Dy (0.73- 0.70) Fe (1.9- 2.0)". J. Appl. Phys., 81 (5) (1997), pp. 2321-2326.

[18] P. Shi et al, "Thermo-magneto-elastoplastic coupling model of metal magnetic memory testing method for ferromagnetic materials", *Journal of Applied Physics*, 123, 145102 (2018)

[19] Hakeim Talleb, Zhuoxiang Ren, A new nonlinear multiscale magnetostrictive approach for FEM modelling of magnetoelectric composites under magneto-thermo-elastic loading, Composite Structures, Volume 303, 2023, 116260, ISSN 0263-8223

[20] L. Bernard, X. Mininger, L. Daniel, G. Krebs, F. Bouillault and M. Gabsi, "Effect of Stress on Switched Reluctance Motors: A Magneto-Elastic Finite-Element Approach Based on Multiscale Constitutive Laws," in IEEE Transactions on Magnetics, vol. 47, no. 9, pp. 2171-2178, Sept. 2011, doi: 10.1109/TMAG.2011.2145387.

[21] L.Sun, X. Zheng, "*Numerical simulation on coupling behavior of Terfenol-D rods, International Journal of Solids and Structures*", vol. 43, Issue 6, 2006,1613-1623,ISSN 0020-7683.

[22] F. C. Graham, C. Mudivarthi, S. Datta, and A. B. Flatau, "Modeling of Galfenol transducer using the bidirectionally coupled magnetoelastic model," *Smart Mater. Struct.*, vol. 18, p. 104013, 2009.

[23] S. Sudersan, A. Arockiarajan, Thermal and prestress effects on nonlinear magnetoelectric effect in unsymmetric composites, Composite Structures, vol. 223,2019,110924,ISSN 0263-8223.

[24] L. Daniel, O. Hubert, "An equivalent stress for the influence of multiaxial stress of the magnetic behavior", *Journal of applied physics* 107, 07A313, 2009.

[25] L. Bernard, X. Mininger, L. Daniel, G. Krebs, F. Bouillault and M. Gabsi, "Effect of Stress on Switched Reluctance Motors: A Magneto-Elastic Finite-Element Approach Based on Multiscale Constitutive Laws," in IEEE Transactions on Magnetics, vol. 47, no. 9, pp. 2171-2178, Sept. 2011, doi: 10.1109/TMAG.2011.2145387.

[26] L. Daniel, "An Analytical Model for the Effect of Multiaxial Stress on the Magnetic Susceptibility of Ferromagnetic Materials", *IEEE Transaction on Magnetics*, vol. 49, no. 5, May 2013.

[27] L. Daniel, " An analytical model for the magnetostriction strain of ferromagnetic materials subjected to multiaxial stress", *Eur. Phys. J. Appl. Phys*, 83, 30904 (2018).

[28] D. Davino, A. Giustiniani, and C. Visone, "Magnetoelastic Energy Harvesting: Modeling and Experiments", in Smart Actuation and Sensing Systems - Recent Advances and Future Challenges. London, United Kingdom: IntechOpen, 2012 [Online]. Available: https://www.intechopen.com/chapters/40055 doi: 10.5772/50892

[29] Valerio Apicella, Carmine Stefano Clemente, Daniele Davino, Ciro Visone, Experimental evaluation of external and built-in stress in Galfenol rods, Physica B: Condensed Matter, Volume 549, 2018, Pages 53-57, ISSN 0921-4526.

[30] Clemente, Carmine Stefano, and Daniele Davino. 2019. "Modeling and Characterization of a Kinetic Energy Harvesting Device Based on Galfenol" *Materials* 12, no. 19: 3199.

[31] A. Mahadevan, P. G. Evans, M. J. Dapino; "Dependence of magnetic susceptibility on stress in textured polycrystalline Fe81.6Ga18.4 and Fe79.1Ga20.9 Galfenol alloys" . *Appl. Phys. Lett.* 4 January 2010; 96 (1) 012502. https://doi.org/10.1063/1.3280374

[32] Bouchilloux, P., Lhermet, N. & Claeyssen, F. Dynamic Shear Characterization in a Magnetostrictive Rare Earth - Iron Alloy. MRS Online Proceedings Library 360, 265–272 (1994). https://doi.org/10.1557/PROC-360-265

[33] Chikazumi, Sōshin (2009). Physics of ferromagnetism. English edition prepared with the assistance of C. D. Graham, Jr. (2nd ed.). Oxford: Oxford University Press. pp. 129–130. ISBN 978-0-19-956481-1.

[34] Wun-Fogle, M.; Restorff, J.B.; Clark, A.E. (2006), "Magnetomechanical Coupling in Stress-Annealed Fe–Ga (Galfenol) Alloys", 42(10), 3120–3122.doi:10.1109/tmag.2006.878394

[35] Hui Jiang, Jie Zhu, Xing Mu, "Grain orientation dependence of ΔE effect and magnetomechanical coupling factor in polycrystalline Galfenol alloy",Computational Materials Science,Volume 156, 2019, Pages 67-76, ISSN 0927-0256.

[36] John L. Butler, “Appication manual for the design of ETREMA Terfenol-D magnetostrictive transducers”, ETREMA Products, Inc., Ames, IA, ©1988
[37] M. Domenjoud et al 2019 Smart Mater. Struct. 28 095012
[38] J. B. Restorff, M. Wun–Fogle, A. E. Clark; Measurement of d15 in Fe100−xGaxFe100−xGax (x=12.5,15,18.4,22)(x=12.5,15,18.4,22), Fe50Co50Fe50Co50, and Fe81Al19Fe81Al19 highly textured polycrystalline rods. J. Appl. Phys. 1 April 2008; 103 (7): 07B305. https://doi.org/10.1063/1.2832667
[39] C.H. Sherman and J.L. Butler, Appendix A.7, p. 555 in Transducers and Arrays for Underwater Sound, Springer, New York, 2007.
[40] Z. Qin, H. Talleb and Z. Ren, "A Proper Generalized Decomposition-Based Solver for Nonlinear Magnetothermal Problems," in IEEE Transactions on Magnetics, vol. 52, no. 2, pp. 1-9, Feb. 2016, Art no. 7400209, doi: 10.1109/TMAG.2015.2492462.
[41] Zienkiewicz, O. C., Zienkiewicz, O. Z., Taylor, R. L., Zhu, J. Z., Nithiarasu, P. (n.d.). The Finite Element Method. Pays-Bas: Elsevier Butterworth-Heinemann.
[42] Hakeim Talleb, Zhuoxiang Ren, «Finite Element Modeling of a Magnetoelectric Energy Transducer Including the Load Effect», IEEE Transactions on Magnetics, vol.51, no.3, pp.1-5, March 2015, doi: 10.1109/TMAG.2014.2357492.
[43] Hakeim Talleb, Zhuoxiang Ren, « Finite element modeling of magnetoelectric laminate composites in considering nonlinear and load effects for energy harvesting», Journal of Alloys and Compounds, vol. 615, 5 December 2014, Pages 65–74., doi:10.1109/TMAG.2015.2487224.
[44] Gilder Nader, Emilio C. N. Silva, and Julio Cesar Adamowski "Determination of piezoelectric transducer damping by using experimental and finite element simulations", Proc. SPIE 5052, Smart Structures and Materials 2003: Damping and Isolation, (31 July 2003); https://doi.org/10.1117/12.483962.

APPENDIX

Appendix A

Magnetization for an isotropic magnetic material subjected to a magnetic field $\boldsymbol{H}$ the direction z (H=Hz) in an orthonormal coordinate system (O,x,y,z) by considering only six domains as possible directions [27].

$$\boldsymbol{M}(H,T) = M_s \frac{A_z \sinh(\kappa \boldsymbol{H})}{A_z \cosh(\kappa \boldsymbol{H}) + A_y + A_x} = M_s \frac{\sinh(\kappa \boldsymbol{H})}{\cosh(\kappa \boldsymbol{H}) + \frac{A_y + A_x}{A_z}} = M_s \frac{\sinh(\kappa \boldsymbol{H})}{\cosh(\kappa \boldsymbol{H}) + \frac{2}{A_{eq}}}$$

$A_i = \exp(\alpha . T_i), i = \{x, y, z\}.$

$$\alpha = \frac{3}{2} \lambda_s A_s$$

$$T_{eq} = \frac{1}{\alpha} \ln\left(\frac{2A_z}{A_y + A_x}\right)$$

$$A_{eq} = \exp(\alpha . T_{eq}) = \exp\left(\alpha . \frac{1}{\alpha} \ln\left(\frac{2A_z}{A_y + A_z}\right)\right) = \frac{2A_z}{A_y + A_x}$$

$$\frac{1}{A_{eq}} = \frac{1}{\exp(\alpha . T_{eq})}$$

Appendix B

$$\partial_T \Lambda|_H = \frac{\partial}{\partial T}\left(\frac{\delta \boldsymbol{H} \kappa(T)}{\tau + (\boldsymbol{H}\kappa(T))^4}\right) = Hu/(\eta T^2)$$

$$\partial_H \Lambda|_T = \frac{\partial}{\partial H}\left(\frac{\delta \boldsymbol{H} \kappa(T)}{\tau + (\boldsymbol{H}\kappa(T))^4}\right) = 1 + u/T$$

$$u = \frac{T^4 \delta \eta^4 (3H^4 - T^4 \tau \eta^4)}{(H^4 + T^4 \tau \eta^4)^2}$$

$$p(\delta, \tau, \eta, H, T) = \boldsymbol{H}\kappa(T) \frac{\delta \boldsymbol{H} \kappa(T)}{\tau + \left(\boldsymbol{H}\kappa(T)\right)^4} + \operatorname{acot}\left(\frac{\left(\boldsymbol{H}\kappa(T)\right)^2}{\sqrt{\tau}}\right)$$

Appendix C

$$c^X = \begin{bmatrix} {c_{11}}^X & {c_{12}}^X & {c_{13}}^X & 0 \\ {c_{21}}^X & {c_{22}}^X & {c_{23}}^X & 0 \\ {c_{31}}^X & {c_{32}}^X & {c_{33}}^X & 0 \\ 0 & 0 & 0 & {c_{44}}^X \end{bmatrix}, X = E \text{ or } B$$

$$\varsigma = \begin{bmatrix} 0 & \varsigma_{31} \\ 0 & \varsigma_{31} \\ 0 & \varsigma_{33} \\ \varsigma_{14} & 0 \end{bmatrix}, \varsigma = e \text{ or } h \text{ or } q$$

$$\eta = \begin{bmatrix} \eta_{11}^S & 0 \\ 0 & \eta_{33}^S \end{bmatrix}, \eta = v^S \text{ or } \varepsilon^S$$

Appendix D

$\alpha_i = r_j z_m - z_j r_m$,
$\beta_i = z_j - z_m$,
$\gamma_i = r_m - r_j$,

Appendix E

$G_A = \xi \mathrm{grad}[N_k]$, $G_u = \mathrm{sym}(\mathrm{grad}[N_k]\,)$, $G_\emptyset = \mathrm{grad}[N_k]$.

$$\boldsymbol{B} = G_A\{\boldsymbol{A}\} = \xi \begin{Bmatrix} -\frac{\partial N_k}{\partial z} \\ \frac{\partial N_k}{\partial r} \end{Bmatrix} \{\boldsymbol{A}\}, \boldsymbol{S} = G_u\{\boldsymbol{u}\} = \begin{bmatrix} \frac{\partial N_k}{\partial r} & 0 \\ N_k/\bar{r} & 0 \\ 0 & \frac{\partial N_k w}{\partial z} \\ \frac{\partial N_k w}{\partial z} & \frac{\partial N_k u}{\partial r} \end{bmatrix} \{\boldsymbol{u}\}$$

It is notice that:
$\frac{\partial N_k}{\partial r} = \beta_k$, $\frac{\partial N_k}{\partial z} = \gamma_k$ and $\frac{N_k}{r} = \alpha_k/\bar{r} + \beta_k + \gamma_k \bar{z}/\bar{r}$

$$\boldsymbol{E} = G_\emptyset\{\emptyset\} = -\begin{Bmatrix} \frac{\partial N_k}{\partial r} \\ \frac{\partial N_k}{\partial z} \end{Bmatrix} \{\emptyset\}$$

Appendix F

Galfenol:
Density (ρ) = 9200 kg.m^{-3}
Elastic constants (pm^2/N): s_{11}^H =220, $s_{33}^H = 190$, s_{13}^H =-82.5
Magnetization saturation Ms=$1.65/\mu_o = 1316$ kA/m
Electrical conductivity: $\sigma = 1.67\mathrm{e}6$ S/m
Reluctivity: $\nu_{\mathrm{ij}}{}^S = \left(\mu_{\mathrm{ij}}{}^S\right)^{-1}$ is extracted from the nonlinear model proposed in section II
Piezomagnetic coefficients (N/Am): $q_{ij}{}^H = c_{ijkl}^H d_{ij}{}^H$, where $d_{ij}{}^H$ is extracted from the nonlinear model proposed in section II

Terfenol-D:
Density (ρ) = 9200 kg.m^{-3}
Elastic constants(pm^2/N): s_{11}^H =27, $s_{33}^H = 42$, s_{13}^H =-19
Magnetization saturation Ms=$1.125/\mu_o = 895.25$ kA/m
Electrical conductivity: $\sigma = 1.1765\mathrm{e}6$ S/m
Reluctivity: $\nu_{\mathrm{ij}}{}^S = \left(\mu_{\mathrm{ij}}{}^S\right)^{-1}$ is extracted from the nonlinear model proposed in section II
Piezomagnetic coefficients (N/Am): $q_{ij}{}^H = c_{ijkl}^H d_{ij}{}^H$, where $d_{ij}{}^H$ is extracted from the nonlinear model proposed in section II

BTO:
Density (ρ) = 6020 kg.m^{-3}
Elastic constants (pm^2/N): s_{11}^E =8.6, $s_{33}^E = 8.93$, s_{13}^E =-2.86
Piezoelectric coefficients (C.m^{-2}): e_{31}=-4.4 , e_{33}=18.6, e_{33}=1.5
Permittivity: $\varepsilon_{31} = \varepsilon_{33} = 1582\varepsilon_O$
Electrical conductivity: $\sigma = 1\mathrm{e}-7$ S/m

PZT-5A:
Density (ρ) = 7750 kg.m^{-3}
Elastic constants pm^2/N: s_{11}^E =16.4, $s_{33}^E = 18.8$, s_{13}^E =-7.22
Piezoelectric coefficients (C.m^{-2}): e_{31}=-7.2, e_{33}=15.12, e_{15}=13.2
Permittivity: $\varepsilon_{31} = \varepsilon_{33} = 1750\varepsilon_O$
Electrical conductivity: $\sigma = 1\mathrm{e}-7$ S/m